CHEMISTRY OF MATERIALS

pubs.acs.org/cm

Article

$Fe_{3-x}InSn_xO_6$ (x = 0, 0.25, or 0.5): A Family of Corundum Derivatives with Sn-Induced Polarization and Above Room Temperature Antiferromagnetic Ordering

Published as part of the Virtual Special Issue "John Goodenough at 100".

Corey E. Frank, Emma E. McCabe, Fabio Orlandi, Pascal Manuel, Xiaoyan Tan, Zheng Deng, Changqing Jin, Mark Croft, Thomas Emge, Shukai Yu, Huaiyu Wang, Venkatraman Gopalan, Saul Lapidus, MeiXia Wu, Man-Rong Li, Juliane Gross, Paul Burger, Aleksandra Mielewczyk-Gryń, Tomasz Klimczuk, Weiwei Xie, David Walker, and Martha Greenblatt*

Cite This: *Chem. Mater.* 2022, 34, 5020−5029

Read Online

ACCESS | Metrics & More | Article Recommendations | Supporting Information

ABSTRACT: Three new double corundum derivative compounds, $Fe_{3-x}InSn_xO_6$ (x = 0. 0.25, or 0.5), were synthesized at high pressure and temperature (6 GPa and 1400−1450 °C). All of the compounds order antiferromagnetically well above room temperature (T_N = 608, 532, and 432 K for x = 0, 0.25, and 0.5, respectively). The x = 0 phase crystallizes as centrosymmetric $R\bar{3}c$, but the inclusion of closed-shell d^{10} Sn^{4+} induces x = 0.25 and 0.5 to crystallize as noncentrosymmetric $R3c$. Microprobe measurements indicate that for x = 0.25 and 0.5, the substitution of Sn^{4+} is not offset by vacancies, which implies the presence of Fe^{2+}, as corroborated by X-ray absorption near-edge spectroscopy and single-crystal X-ray structure refinements. Neutron powder diffraction experiments on x = 0.5 indicate that these compounds are canted A-type antiferromagnets that, like Fe_2O_3 and $InFeO_3$, consist of ferromagnetic layers that stack antiferromagnetically with a single magnetic transition. Weak ferromagnetic interactions persist to very high temperatures. Temperature-dependent second harmonic generation (SHG) measurements on x = 0.25 and 0.5 show a SHG response with ferroelectric-like hysteretic maxima that correspond with the respective magnetic transitions, which suggest coupling of the magnetic and polarization order. These new compounds provide more information about fine-tuning the electronic, magnetic, and structural properties of corundum-derived mutlferroics in the search for tunable high-temperature magnetoelectric materials.

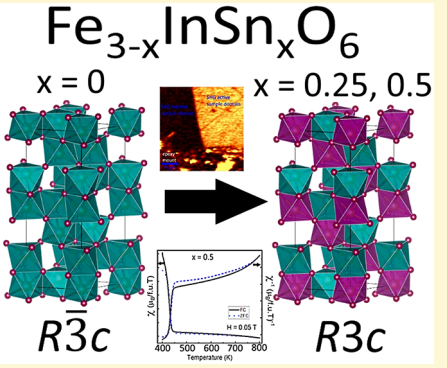

INTRODUCTION

Multiferroic materials, with more than one type of stable, switchable long-range order such as ferromagnetism and ferroelectricity, are of significant interest from the perspective of both applications and fundamental science.[1,2] From complex fundamental phenomena to practical applications in microwave tuners and field sensors, multiferroics, and especially magnetoelectrics in which order parameters are cross coupled, have a great impact on modern life.[3−5] Nevertheless, predicting materials with these properties, and fine-tuning them through synthesis, has proven to be a significant challenge.[6]

A majority of multiferroic materials, both in theory and in application, thus far have been of the ABO_3 or $A_2BB'O_6$ perovskite structure type.[6] In a perovskite, a large A cation is 12-fold coordinated by oxygens and fits into the vacancies of a three-dimensional array of corner-sharing BO_6 octahedra. The stability of a perovskite at ambient pressure is roughly predicted by the Goldschmidt tolerance factor, t [$t = \frac{R_A + R_O}{\sqrt{2}(R_B + R_O)}$, where RA and RB are the radii of the A and B cations, respectively, and R_O is the radius of the oxygen anion]; t = 1 for a "perfect" cubic perovskite. As first noted in the seminal perovskite ferroelectric, $BaTiO_3$,[7] ferroelectricity in perovskites is often driven by hybridization of oxygen 2p electrons with the empty d orbitals on the B-site cations, leading to polar displacements. This electronic driving force is therefore less favorable for (magnetic) transition metal cations with electrons in the d shell. The rational design of perovskite multiferroics is a Herculean task at best, and new design strategies and mechanisms are attracting more attention.[8−11]

Recently, high-pressure, high-temperature (HPHT) synthesis has allowed the exploration of corundum (ABO_3) and

Received: January 30, 2022
Revised: May 18, 2022
Published: June 2, 2022

double corundum ($AA'BB'O_6$) structural families ($t < 0.85$) as an alternative archetype to the traditional perovskite.[12−17] In corundum, face-sharing dimers of AO_6 and/or BO_6 octahedra along the c axis form edge-sharing layers in the $a-b$ plane. Specific subtypes (such as the eponymous corundum $R\bar{3}c$ and $LiNbO_3$ $R3c$ types) are distinguished by the pattern of dimers to vacancies along the [001] direction. While there are some exceptions, HPHT synthesis techniques are typically required to stabilize these low-t materials.[18−22] The key to ferroelectric polarization in corundum lies in the dimers. Coulombic repulsions between the A and B cations of different sizes and/or charges cause local polarization when cations are displaced by different magnitudes from the shared face. Ferroelectric switching occurs when a cation from one dimer migrates through an O_3 face to fill a former vacancy, forming a new dimer with the A/BO_6 octahedron that had previously been separated by a vacancy, leaving a new vacancy in its place.[10] An empty d shell is not required for this migration, and therefore, magnetic cations can be inserted in any A/A' or B/B' site.[10,23,24] For example, Mn_2FeMoO_6, a polar double corundum ferrimagnet with a T_N above room temperature (337 K), has magnetic cations on both the A (d^5 Mn^{2+}) and B (d^5 Fe^{3+} and d^1 Mo^{5+}) sites.[17] Other known polar corundum-type materials with T_C and T_N values above room temperature reported thus far include $LiNbO_3$-type $BiFeO_3$ ($R3c$; T_N = 643 K),[25] $ScFeO_3$ ($R3c$; T_N = 356 K),[26] $GaFeO_3$ ($R3c$; T_N = 408 K),[27] and $InFeO_3$ ($R3c$; T_N = 545 K).[28] To the best of our knowledge, other reported corundum and double corundum oxides either are centrosymmetric or have a T_C or T_N below room temperature.[2]

In this work, we present $Fe_{3-x}InSn_xO_6$ (x = 0, 0.25, and 0.5), a family of double corundum-related compounds made at HPHT (6 GPa and 1400−1450 °C). Fe_3InO_6 has been found to be centrosymmetric $R\bar{3}c$ through second harmonic generation (SHG) investigations, but the inclusion of a small amount of closed-shell Sn^{4+} causes the x = 0.25 and 0.5 compounds to order in a $LiNbO_3$-type $R3c$ polar structure at less than half of the pressure required to synthesize the most similar compound above, $InFeO_3$ (1450 °C and 15 GPa),[28] and to show a hysteretic SHG response with maxima near their respective magnetic transitions. While it would be reasonable to assume that the incorporation of Sn^{4+} must be charge-balanced by Fe^{3+} or In^{3+} vacancies, electron microprobe studies indicate practically ideal stoichiometries for all species, and X-ray absorption near-edge spectroscopy indicates the presence of Fe^{2+}. Additionally, in 2010, Gauden et al. investigated the doping of Sn^{4+} and co-doping of Mg^{2+} and Sn^{4+} into antiferromagnetic hematite ($R\bar{3}c$ Fe_2O_3) itself and found that the inclusion of Mg^{2+} stabilized the lattice more effectively than Sn^{4+} balanced by Fe^{3+} vacancies (maximal degree of substitution of ∼10% Sn).[29] For these reasons, we find it reasonable to hypothesize that Sn^{4+} in $Fe_{3-x}InSn_xO_6$ is offset by some amount of Fe^{2+}. The work presented here aims to improve the overall understanding of ferroelectricity and possible tuned multiferroicity in above room temperature magnets in the corundum structure archetype.

EXPERIMENTAL SECTION

Synthesis. Powders of SnO_2 (Sigma-Aldrich, 99.9%) and Fe_2O_3, In_2O_3, and Fe (Alfa Aesar, 99.998%, 99.99%, and 99.9%, respectively) were weighed in stoichiometric quantities and ground in an agate mortar. The mixed powders were wrapped in platinum foil pressurized to 6 GPa in a Walker-type multi-anvil apparatus over 8−12 h and then heated to 1400−1450 °C for 0.5−2 h, with longer times preferred to promote the growth of larger single crystals (≤1 mm) and shorter times optimized to preserve aggregated dense pellets (appropriate for the measurement of certain properties). Samples were quenched by turning off the power to the heater and depressurized over the course of several hours.

Synchrotron X-ray Diffraction. Samples were finely ground and characterized by synchrotron powder X-ray diffraction (SPXD) at Argonne National Laboratory's Advanced Photon Source, beamline 11-BM (λ = 0.412749 Å), via the mail-in service. Structural refinements were performed with TOPAS Academic and GSAS-II software.

X-ray Diffraction. Initial powder X-ray diffraction (PXD) was performed on ground crystals with a Bruker D8 Advance diffractometer. Single-crystal X-ray data (SCXD) were collected with Mo Kα radiation (λ = 0.7107 Å) at room temperature on a single crystal (0.040 mm × 0.020 mm × 0.010 mm) on a Bruker Smart APEX system with a charge-coupled device (CCD) area detector and monocapillary collimation. The reflection data were corrected for polarization and Lorentz and absorption effects, the latter by use of a multiscan method with Bruker program TWINABS. Crystallographic details, including transmission factor ranges, are available in the Supporting Information. The structure was determined with SHELXT and refined with SHELXL.[30−32]

Microprobe. Polycrystalline pressed pellets and large single crystals were embedded into epoxy resin and ground flat on one side before being coated with a thin layer of carbon. Analyses were performed in both point-select and multiline scan modes on a JEOL JXA Superprobe at Rutgers University or on a Cameca SX-100 instrument with a Princeton Gamma Tech IMIX energy dispersive spectrometer at the American Museum of Natural History in New York.

Second Harmonic Generation (SHG). SHG measurements were performed on a modified Kurtz-NLO system, using a Ti Sapphire regenerative amplifier laser with a central wavelength of 800 nm, a repetition rate of 1 kHz, and a pulse duration of <100 fs. No index matching fluid was used in any of the experiments. Temperature-dependent measurements were recorded during both heating and cooling for polycrystalline pressed pellets of x = 0.25 and 0.5 in three sweeps from 300 to 773, 973, and 1073 K for x = 0.25 and two sweeps both from 300 to 575 K for x = 0.5. Subsequent electron backscatter diffractometry (EBSD) experiments were performed with an Apero 2 scanning electron microscope.

X-ray Absorption Near-Edge Spectroscopy (XANES). XANES data were collected simultaneously with standards in both transmission and fluorescence modes on beamline 7-BM (QAS) using a Si(111) channel cut monochromator at Brookhaven National Laboratory's National Synchrotron Light Source (NSLS-II). The standard analysis methods, of pre/post-edge background subtraction and normalization to the unity absorption step at the edge, were used in the data analysis

Magnetic Measurements in a Finite Field. Magnetization measurements were carried out in a magnetometer with a superconducting quantum interference device (SQUID). Field-cooled (FC) and zero-field-cooled (ZFC) magnetic measurements were taken in the temperature range of 5−400 K with an applied magnetic field of 1 T and in the range of 400−800 K at 0.5 T. Isothermal magnetization curves were obtained at 5, 100, 150, and 300 K under an applied magnetic field ranging from 6 to −6 T.

Specific Heat Capacity. High-temperature (35−545 K) specific heat measurements were performed at the Institute of Nanotechnology and Materials Engineering (Gdansk University of Technology) by a Netzsch DSC 204 F1 Phoenix system. Measurements were taken in Al concave crucibles on an 18 mg bulk sample; the system was calibrated with prior sapphire measurements and purged by air during measurements.

Neutron Powder Analysis of x = 0.5. Time-of-flight neutron powder diffraction (NPD) data were collected for x = 0.5 on the WISH diffractometer at the ISIS Neutron and Muon Source.[33] The sample (0.1216 g) was loaded into a 6 mm diameter cylindrical

https://doi.org/10.1021/acs.chemmater.2c00312
Chem. Mater. 2022, 34, 5020−5029

vanadium can sealed with a copper O-ring. Thirty minute scans were collected at 300 K and then at 50 K intervals up to 500 K. The sample was then cooled, and data were collected at 5 K and then at 15 K intervals on warming to 300 K. Rietveld refinements[34] were carried out with TopasAcademic software[35,36] using the higher-resolution banks of data (average 2θ values of 152.8° and 121.6° spanning a d spacing range of ~0.7−5.2 Å), and no peaks with larger d spacing were observed in smaller-angle banks of data in the temperature range studied. ISODISTORT[37] was used to explore possible magnetic structures. Traces of impurity phases SnO_2 and $InFe_2O_4$ were identified in NPD data and modeled by Pawley phases. Peaks due to Al from the sample environment were also present in larger-angle NPD (2θ = 152.8°) data, and these were fitted with two Pawley phases.

RESULTS AND DISCUSSION

Synchrotron powder diffraction on $Fe_{3-x}InSn_xO_6$ (x = 0, 0.25, and 0.5) indicates that x = 0, 0.25, and 0.5 crystallize in either centrosymmetric $R\bar{3}c$ or noncentrosymmetric $R3c$ [for x = 0, 0.25, and 0.5, a = 5.1526 Å and c = 13.9359 Å, a = 5.1832 Å and c = 13.9986 Å, and a = 5.2125 Å and c = 14.0620 Å, respectively (see Figure 1 and the Supporting Information)].

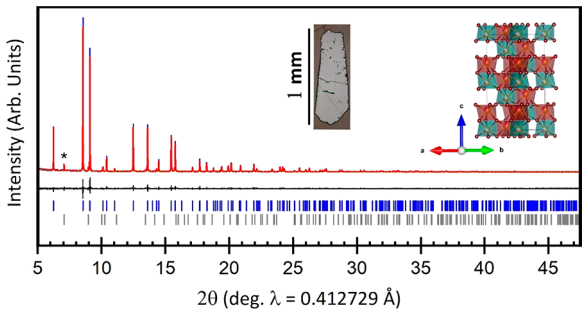

Figure 1. Refinement of $Fe_{3-x}InSn_xO_6$ (x = 0.5) SPXD data in $R3c$. The experimental pattern is colored blue, the calculated pattern red, and the difference gray. Blue ticks indicate the main phase, with an SnO_2 impurity in gray ticks (main peak indicated with asterisk). The inset is an image of one of the crystals grown at HPHT, showing optically continuous anisotropy on a 1 mm scale (left) and the $R3c$ structure viewed along the a−b plane (right).

Due to limitations of the twin operation of Friedel's law, these space groups[38] cannot be distinguished by powder diffraction. Subsequent single-crystal experiments indicated that there was an approximately equal electron density on both metal sites, implying that there is an equal distribution of iron on the A and B sites. Additionally, structure factor analyses showed that while x = 0 should reasonably be assigned $R\bar{3}c$, x = 0.25 or 0.5 showed either a noncentrosymmetric or a hypercentric distribution, respectively. In Rietveld refinements, x = 0.25 and 0.5 species refined acceptably to either $R\bar{3}c$ or $R3c$ (wR^2 difference of ~0.5%). Some of this uncertainty, especially concerning structure factors, could be attributed to twinning as these HPHT synthesized samples were seen to be highly susceptible to obverse−reverse twin intergrowths. To determine whether x = 0.25 and 0.5 were centrosymmetric or noncentrosymmetric, x = 0, 0.25, and 0.5 were analyzed via SHG, which will be discussed in detail shortly, which agreed with single-crystal structure factor analyses. Therefore, x = 0 was finally assigned $R\bar{3}c$ and x = 0.25 and 0.5 were assigned $R3c$ for final SPXD refinements.

X-ray absorption near-edge spectroscopy (XANES) was employed to probe cation valences and their potential Sn substitution-induced changes in the title compound series. With regard to Figure 2a, one should note the well-known systematic chemical shift of the Fe−K main edge to higher energy in the Fe^{2+}−Fe^{3+}−Fe^{4+} sequence of standard compound spectra. This edge energy upshift with increasing valence is ubiquitous in XANES measurements and reflects the increase in binding energy with a decrease in the level of screening. Although the local structure contributes to the detailed spectral edge shape, the chemical shift effect remains apparent. It should be noted that the rapid spectral rise demarcating the chemical shift for the x = 0 spectrum is consistent with Fe^{3+} and that the x = 0.5 spectrum is very clearly shifted somewhat down in energy.

Figure 2b displays the Fe−K pre-edge region, where transition features involving final d-states (quadrupole allowed) and d−p hybridized states (dipole allowed) are observed. Here the Coulomb attraction energy between the core hole and final d-state shifts these transitions down into the pre-edge region. Both the structure and the chemical shift of these features serve as confirming indicators of Fe-valence changes. There is a spectral evolution from a low-energy peak feature in the Fe^{2+} standard spectra to a bimodal higher-energy peak feature in the Fe^{3+} standard and to a higher-intensity/energy feature in the Fe^{4+} standard; the bimodal character and chemical shift of the x = 0 pre-edge spectrum are consistent with its Fe^{3+} character. It should be noted that in comparison the x = 0.5 pre-edge spectrum is broadened on its low-energy side, consistent with a modest Fe^{2+} admixture as in the main edge results.

Panels c and d of Figure 2 display the Sn and In K edges of these materials. The K edges of these p-block materials manifest both the typical chemical shift to higher energies with an increase in valence and valence-coupled modifications in the near-edge peak feature intensity (involving dipole transitions into final p-states). In Figure 2c, the increased chemical shift and peak intensity between elemental Sn^0 and $Sn^{4+}O_2$ are clear. The close correspondence between the $Sn^{4+}O_2$ and the x = 0.5 and 0.25 spectra unambiguously establishes the Sn^{4+} character of the substitution (the x = 0.25 spectrum has been shifted for the sake of visibility; otherwise, the x = 0.5 and 0.25 spectra perfectly overlap). Similarly, in Figure 2d the close correlation between the $In^{3+}{}_2O_3$ x = 0 and 0.5 spectra establishes a constant In^{3+} state in the latter two. Thus, the XANES results imply that the Sn^{4+} substitution is offset by some Fe^{2+} admixture, and this was used, in combination with electron microprobe results (Figure S4), as justification for fixing all sites as fully occupied in SCXRD and SPXD Rietveld refinements.

As mentioned, second harmonic generation was utilized for final space group assignation of $Fe_{3-x}InSn_xO_6$. SHG is an even-order nonlinear optical technique that is sensitive to symmetry, especially the presence of an inversion center that destroys the SHG phenomenon.[39] At room temperature, x = 0.25 and 0.5 both showed some degree of illumination when exposed to a linearly polarized incident beam, which indicates that both samples could be noncentrosymmetric, whereas x = 0 showed no SHG signal and was thus assigned centrosymmetric $R\bar{3}c$ (Figure S3). Much of the SHG-active portion of x = 0.25 was seen to be at grain boundaries, which could be an indication of surface irregularities or strain effects, so further investigation was warranted.

It is well established that the intensity of the SHG response is proportional to nonlinear polarization in SHG-active

https://doi.org/10.1021/acs.chemmater.2c00312
Chem. Mater. 2022, 34, 5020−5029

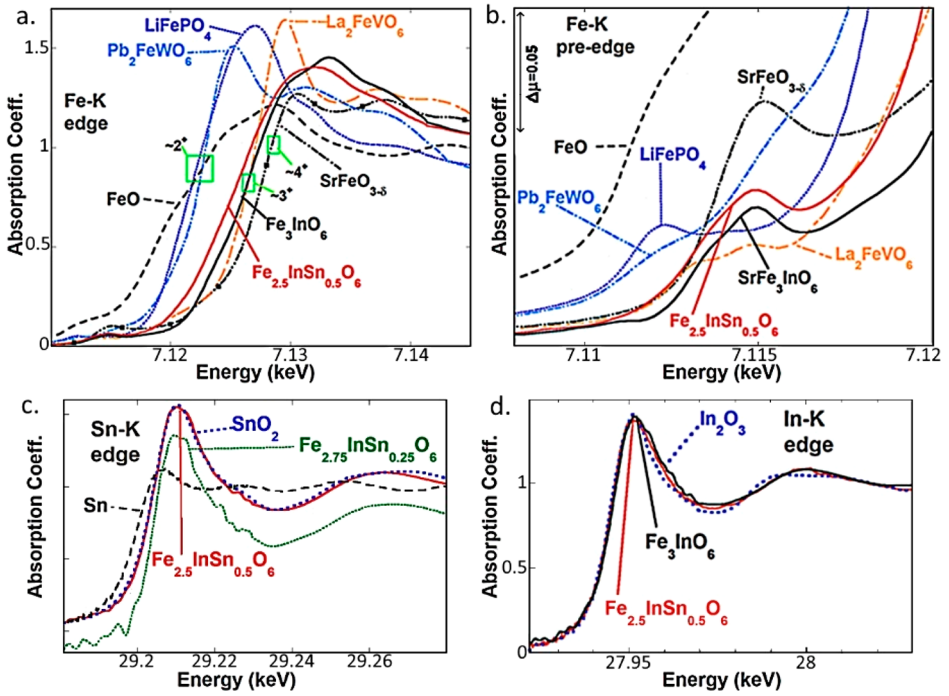

Figure 2. (a) Fe K edge for $Fe_{2.5}InSn_{0.5}O_6$ (solid red) and various standards, $Fe^{2+}O$, $Pb_2Fe^{2+}WO_6$, $LiFe^{2+}PO_4$, $(Fe^{3+})_3InO_6$, $La_2Fe^{3+}VO_6$, and $SrFe^{4+}O_{3-\delta}$, for comparison. (b) Fe K pre-edge of $Fe_{2.5}InSn_{0.5}O_6$ with the same standards as in panel a. (c) Sn K edge of $Fe_{2.5}InSn_{0.5}O_6$ (solid red) and $Fe_{2.75}InSn_{0.25}O_6$ (dashed green, displaced down) compared to those of Sn^0 and $Sn^{4+}O_2$ (note that the $x = 0.25$ spectrum has been displaced for the sake of visibility as it overlaps with the $x = 0.5$ spectrum). (d) In K edge of $Fe_{2.5}InSn_{0.5}O_6$ and Fe_3InO_6 compared to that of $In^{3+}{}_2O_3$.

materials and that in ferroelectrics this response is dependent on both time and temperature.[40,41] As shown in Figure 3,

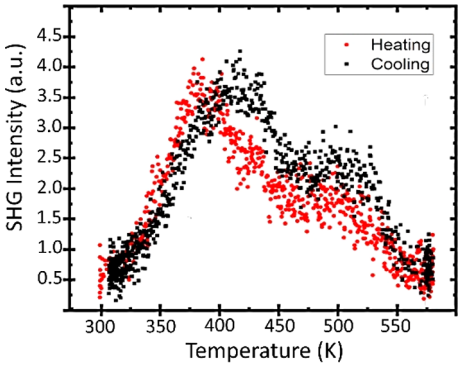

Figure 3. Temperature-dependent second harmonic generation data for $x = 0.5$ during heating (red circles) and cooling (black squares) showing a maximum response between 400 and 450 K, near the magnetic transition (T_N = 432 K).

temperature-dependent measurements for $x = 0.5$ [T_N = 432 K (*vida infra*)] show an SHG response that increases with temperature to a maximum between 400 and 450 K, a behavior that indicates not only that there are polarizable domains in $x = 0.5$ but also that these domains increase their polarization with the application of temperature. The smooth transition is nearly identical during heating and cooling, similar to hysteresis observed previously in some ferroelectric materials. There is a second, smaller, and more dispersed peak at approximately 525 K in $x = 0.5$ that is reminiscent of the dielectric permittivity anomaly seen in low-frequency dielectric measurements of relaxor ferroelectrics. However, several other possible explanations may be more appropriate, including a second polar phase transition, as in the case of $LiRbSO_4$,[42] other effects such as an anomaly in the linear dielectric function at optical frequencies (as the SHG intensity is approximately proportional to the third power of the linear refractive index), domain reorientations in the sample, or potentially some $x = 0.25$ contamination (due to its position and relative size). The somewhat broad dispersion in both peaks can reasonably be attributed to sample effects, which was a polycrystalline pressed pellet with grains in a random, as-grown orientation. As *R*3*c* (point group 3*m*) is optically uniaxial, SHG should be observed only when the incident polarization has a component along the *c* axis of $x = 0.5$.[43]

A similarly smooth thermal hysteresis is seen in $x = 0.25$ (Figure 4). Because the room-temperature SHG signal in $x = 0.25$ seemed strongest at grain boundaries and surface defects, temperature-dependent SHG measurements were performed in three sweeps on a different polycrystalline sample to rule out strain or surface effects. Each sweep shows a broad maximum similar in shape to that of $x = 0.5$. The maximum response occurs at approximately 550 K for sweeps 1 and 3, which corresponds with the magnetic transition (T_N = 532 K, which will be discussed shortly). Major features for sweep 2 are displaced by ~150 K relative to the other sweeps (Figure 4b); however, several possibilities exist to explain this displacement, including hysteretic effects in polycrystalline samples and the change in laser focus leading to a drift of the sampled region of polycrystalline grains.

The peak in SHG activity at 400−450 K for $x = 0.5$ (Figure 3) and at approximately 550 K in $x = 0.25$ (Figure 4) could indicate a change in the polarization of these materials at their respective temperatures, perhaps related to the onset of antiferromagnetic order below 432 and 532 K, respectively (Figure 5). The SHG activity at high temperatures (and the suggestion of Sn order from the 500 K NPD data of $x = 0.5$)

https://doi.org/10.1021/acs.chemmater.2c00312
Chem. Mater. 2022, 34, 5020−5029

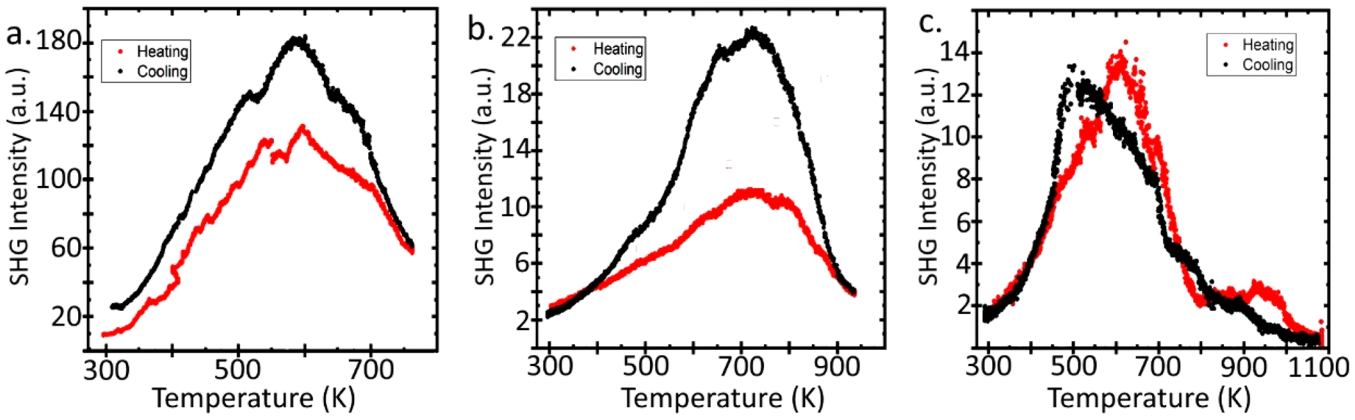

Figure 4. Temperature-dependent second harmonic generation data for $x = 0.25$ during heating (red) and cooling (black) in sweeps from 300 K to (a) 773 K, (b) 973 K, and (c) 1073 K showing a maximum response in all three sweeps. The displacement of the second sweep (b) is most likely attributed to measurement effects or to hysteretic effects in the polycrystalline samples.

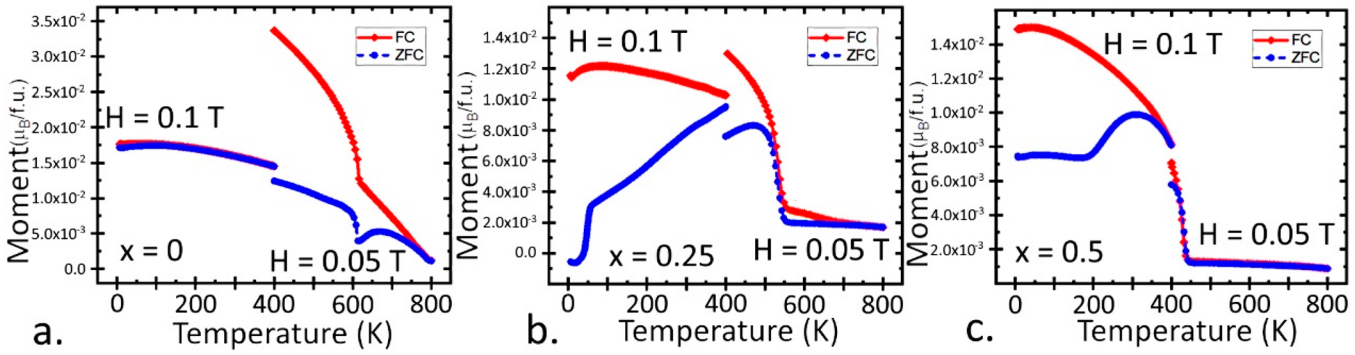

Figure 5. Magnetization vs temperature curves for (a) $x = 0$, (b) $x = 0.25$, and (c) $x = 0.5$ showing sharp transitions at 608, 532, and 432 K, respectively. (The apparent second transition at 50 K in panel b is an artifact of oxygen freezing.) The FC and ZFC curves diverge to some degree after T_N, implying the possibility of frustration, and linear Curie−Weiss behavior is not observed above T_N up to 800 K, the limit of measurement. Measurements had to be performed in two sets: the first from 0 to 400 K (at $H = 0.1$ T) and the second from 400 to 800 K (at $H = 0.05$ T) due to limitations with the SQUID heating attachment. The differences in FC/ZFC divergence for panel a and for 0−400 K for panel b can be attributed to the fact that the 0−400 K trial did not heat the sample above the magnetic transition.

suggests that $x = 0.5$ and by extension $x = 0.25$ adopt the noncentrosymmetric $R3c$ structure in the entire temperature range studied. Therefore, magnetic order is not needed to explain the loss of inversion symmetry (this is broken by the existing Sn−Fe/In cation order), but magnetic order could still cause a change in polarization in this material. Similar coupling between magnetic order and polarization, caused by magnetostriction, has been observed in corundum-derived Mn_2MnWO_6 ($R3$, $T_N = 58$ K, spontaneous polarization $\cong 63.3\ \mu C\ cm^{-2}$).[18] The origin of this coupling was clear from the structural changes observed upon cooling through this transition. This contrasts with $Fe_{2.5}InSn_{0.5}O_6$ for which the nuclear structure seems to change smoothly with an increase in temperature (see the Supporting Information), although further data points close to the transition temperature would be required to rule out such coupling.

Magnetization versus temperature, $M(T)$, experiments were performed in two sets for all samples: the first from 0 to 400 K with $H = 0.1$ T and the second from 400 to 800 K with $H = 0.05$ T. (Two sets of measurements were required as a heating attachment must be fitted to the magnetometer to measure above 400 K.) In all cases, there is a sharp transition at T_N [608, 532, and 432 K for $x = 0$, 0.25, and 0.5, respectively (Figure 5)], which is well above room temperature and which at first appears to be ferro- or ferrimagnetic. This implies that there are weak ferromagnetic or canted antiferromagnetic interactions present even at very high temperatures, similar to what is seen in hematite.[44] In none of the three species is linear Curie−Weiss behavior seen, up to instrument limitations. Instead, there is curvature that increases as the transition temperature approaches. At the highest measurement temperatures, the zero-field-cooled (ZFC, blue circles) and field-cooled (FC, red squares) curves overlap but then soon begin to diverge as the sample is cooled. This divergence is most pronounced in $x = 0$, where it begins at ∼725 K, and in $x = 0.25$, where it begins at ∼650 K. For $x = 0.5$, the ZFC and FC curves do not begin to diverge until below T_N. Magnetization versus field, $M(H)$ (Figure 6 and Figure S6), experiments were performed at various temperatures below 300 K. The magnetization of all species is seen to be low (0.14 μ_B/formula unit for $x = 0.5$ as shown in Figure 6, for example) and unsaturated at the limits of measurement, typical for antiferromagnetic exchange. For $x = 0.5$, the largest coercive field ($H_c \sim 0.77$ T) is observed at the lowest measurement temperature. While coercivity does decrease with an increase in temperature somewhat from 300 to 200 K, it remains, indicating the continued presence of ferromagnetic or canted ferromagnetic-like interactions. There is no indication in any case of a metamagnetic transition such as spin flop or spin flip up to $H = 6$ T. $M(H)$ could not be measured above the

https://doi.org/10.1021/acs.chemmater.2c00312
Chem. Mater. 2022, 34, 5020−5029

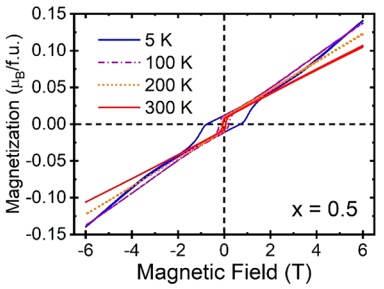

Figure 6. Magnetization vs field, $M(H)$, for $x = 0.5$ from $H = -6$ T to $H = 6$ T for 5, 100, 200, and 300 K.

transition temperature due to limitations of the magnetometer heating attachment.

Let us for a moment consider hematite ($R\bar{3}c$ Fe_2O_3) as an archetype of both of our compounds and other Fe^{3+}-containing corundums such as $ScFeO_3$,[26] $GaFeO_3$,[27] and $InFeO_3$,[28] perhaps understanding them best as dilutions of the same. Below T_N (≈948 K), hematite is a canted antiferromagnet. Spins order in ferromagnetic layers that stack antiferromagnetically along the c axis.[45] A small macroscopic magnetic moment (0.0144 μ_B/formula unit)[44,46−48] is observed until just above the Morin transition, T_M. After T_M, pure hematite becomes perfectly antiferromagnetic.[44] The Morin transition can be suppressed by substituting nonmagnetic metals into the lattice, disrupting Fe−O−Fe superexchange, as in the cases of Sn^{4+}-doped and Sn^{4+}- and Mg^{2+}-codoped hematite studied by Gaudon et al.[29]

In our "dilution" compounds, one might expect that the strength of macroscopic magnetic exchange would decrease smoothly with the decrease in magnetic carriers. This is seen in $Fe_{3-x}InSn_xO_6$ (Figure 7); however, $InFeO_3$ (T_N = 545 K), $GaFeO_3$ (T_N = 408 K), and $ScFeO_3$ (T_N = 356 K) all have different T_N values despite having a 50/50 M^{3+}/Fe^{3+} cation ratio. The reduction in T_N in these three polar double corundum compounds instead seems to roughly correlate with the increasing deviation of the corner-sharing M−O−M angle from the ideal value of 180° (138.5°, 130.0°, and 129.4°, respectively), which has been previously pointed out in comparison with similar perovskite phases.[49] $Fe_{3-x}InSn_xO_6$ does not seem to follow this rule. The equivalent M−O−M interlayer exchange angle (Table S3) is 131.4(3)° and 131.7(4)° (for the site with Sn) or 131.2(3)° and 131.3(4)° (for the one without) for $x = 0.25$ and 0.5, respectively. Both $x = 0.25$ and $x = 0.5$ have transition temperatures that are lower than that of $x = 0$ but larger corner-sharing angles [131.20(6)° for $x = 0$]. A crucial difference between $x = 0$, 0.25, and 0.5 and the other species discussed is the nearly equal distribution of magnetic cations on the A and B sites. This seems to lead to greater magnetic exchange between layers than in $InFeO_3$, $GaFeO_3$, or even $ScFeO_3$ (which is almost in line with our linear distribution) in which M^{3+} and Fe^{3+} do not site-share, and thus a higher T_N.

It is clear that the precipitous drop in T_N from $x = 0$ to $x = 0.5$ cannot be attributed to a "perovskitic" octahedral tilt angle[50,51] analysis. These species all have Fe mixed in the A and B sites, and similarly small M−O−M angles. The difference between them is the number of closed-shell d^{10} ions (In^{3+} and Sn^{4+}) admixed in sites A and B. Closed-shell d^{10} cations on the B and B' sites of antiferromagnetic perovskites have been demonstrated to weaken overall magnetic exchange interactions,[52] which should reduce T_N. As the increase in the percent of closed-shell cations is the least subtle differing factor (other than space group, which does not seem to effect T_N when going from $x = 0$ to $x = 0.25$ thus far), yet the transition temperatures fall by approximately 100 K as the d^{10} content increases, it appears that this phenomenon applies to the corundum structure family as well.

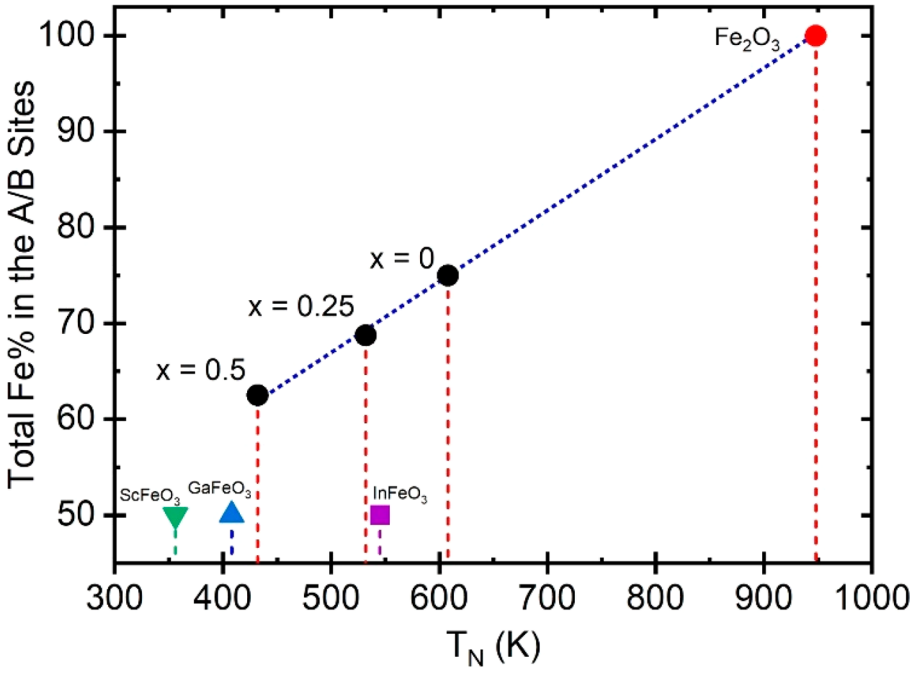

Figure 7. Plot of the percent Fe content vs transition temperature for $x = 0$, 0.25, and 0.5 (black circles) compared to those of Fe_2O_3[44] (T_N = 948 K, red circle), $InFeO_3$[28] (T_N = 545 K, purple square), $GaFeO_3$[27] (T_N = 408 K, blue triangle), and $ScFeO_3$[26] (T_N = 356 K, green triangle). The blue line is a guide to the eye.

https://doi.org/10.1021/acs.chemmater.2c00312
Chem. Mater. 2022, 34, 5020−5029

Specific heat measurements were performed on a dense polycrystalline pellet of $x = 0.5$. As shown in Figure 8, there is a distinct transition at 410 K, the position of which correlates reasonably well with the maximum response seen in the temperature-dependent SHG of $x = 0.5$ (Figure 3) and T_N (432 K). No second anomaly or discontinuity is seen near the peak of the specific heat that would correspond to the anomalous second peak in the temperature-dependent SHG at ~525 K. Thus, the specific heat indicates that the phase transition at 410 K dominates and strongly implies that the magnetic transition and the maximum SHG response are coupled.

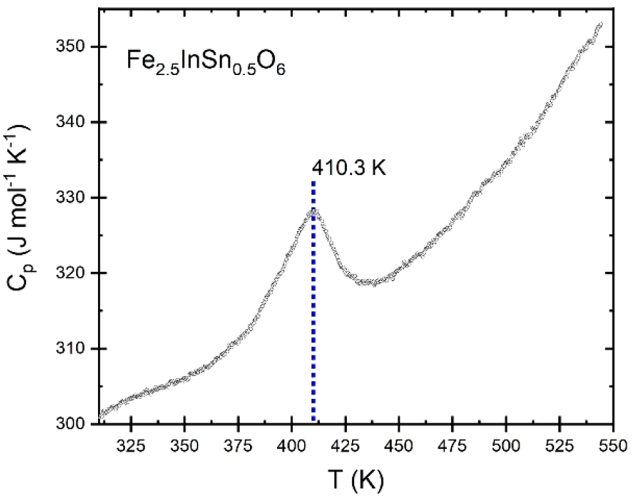

Figure 8. Temperature-dependent specific heat C_p of $Fe_{2.5}InSn_{0.5}O_6$ in the vicinity of the transition. A distinct transition can be seen at 410 K, and no additional anomaly or discontinuity is observed in the vicinity of the anomalous second peak in the SHG measurements [~525 K (Figure 3)].

Time-of-flight neutron powder diffraction (NPD) data of $Fe_{2.5}InSn_{0.5}O_6$ were recorded to understand the magnetic order and to determine the distribution of Sn between the *A* and *B* metal sites.[1] In, Fe, and Sn have contrasting neutron scattering lengths (4.065, 9.54, and 6.2257 fm, respectively), meaning neutrons, unlike X-rays, are sensitive to potential Sn site ordering. SCXRD data were used to determine the initial distribution of Fe and In/Sn over the two 6a sites of the *R*3*c* model. Refinement of 500 K data suggested only a slight ordering of Fe over the two sites [Fe occupancies of 0.59(1) and 0.66(1) were obtained for cation sites *A* and *B* (see the Supporting Information)]. In subsequent refinements, Fe-site occupancies were fixed and constraints were used to maintain stoichiometry (a single global temperature factor was used for all sites); otherwise, In and Sn were allowed to refine freely. These refinements suggest that In and Sn are almost completely ordered, with Sn preferring the slightly smaller coordination octahedron. The final refinement profiles and full details are given in the Supporting Information. It should be noted that an acceptable fit was also obtained for an $R\bar{3}c$ model, but this would not be consistent with SHG measurements. Moreover, it would be surprising given that $InFeO_3$ was recently reported to be noncentrosymmetric.[8]

Below $T_N = 432$ K, strong additional Bragg reflections are observed and, as shown in the Supporting Information, increase smoothly upon cooling. These reflections can be indexed by a magnetic cell with the same dimensions as the nuclear unit cell (e.g., 003 peak at 4.69 Å; 101 peak at 4.30 Å), suggesting a magnetic propagation vector $\mathbf{k} = (0\ 0\ 0)$. Possible magnetic structures were explored using the web-based ISODISTORT software.[5] Consideration of possible magnetic ordering modes using mode inclusion analysis[7] suggested that a good fit was obtained for models with moments in plane described by $m\Gamma_3$ modes on both Fe sites (Supporting Information), analogous to the magnetic structure reported for $InFeO_3$.[8]

Two similar magnetic structures that differ in the arrangement of Fe moments in (001) planes and allowed out-of-plane components are possible: a model of *Cc* symmetry with moments along [210] relative to the nuclear unit cell, with an out-of-plane antiferromagnetic component (described by irrep $m\Gamma_1$) also allowed by symmetry, or a model of *Cc*′ symmetry with moments along [100] relative to the nuclear unit cell, with an out-of-plane ferromagnetic component (described by irrep $m\Gamma_2$).

These two models both allow for the existence of the observed weak ferromagnetic moment perpendicular to the main AFM direction, and both give equivalent fits to the data (Supporting Information) that cannot be distinguished by powder diffraction experiments.[53] Single-crystal measurements (e.g., polarized neutron diffraction or magnetization measurements on single crystals) would be needed to distinguish unambiguously between these models.

Refinements suggested moments of similar magnitudes on both Fe sites, so constraints were used to impose equal moments. The first model of *Cc* symmetry was used in all further analysis. Refinement using 5 K data indicated moments of 3.88(1) μ_B per Fe, lower than that expected for high-spin d^5 Fe^{3+} ions (5.92 μ_B), likely due in part to the reduction of some iron to Fe^{2+} as Sn^{4+} is accommodated by the system. The reduction in the ordered moment could also result from covalency, frustration in the magnetic interactions of canted moments, complex domain effects in the sample, disorder in the nuclear structure, or a combination of these effects. Moments are predominantly in the (001) planes, but allowing the out-of-plane AFM component [0.51(6) μ_B] gives a very slight improvement in fit (R_{wp} decreases from 2.24% to 2.23% for this additional parameter); however, this cannot be confirmed from these data. Refinement profiles and full details are given in Figure 9 and Table S4, and the magnetic structure is illustrated in Figure 10.

This magnetic structure suggests that AFM exchange between Fe^{3+} ions across the shared face of the AO_6−BO_6 dimers dominates the magnetic ordering, leading to FM layers that are stacked antiferromagnetically along [001], similar to collinear β-Mn_2InSbO_6.[54] Sequential Rietveld refinements suggest a smooth increase in unit cell volume upon warming (see the Supporting Information). There is no evidence of a change in magnetic structure, or magnetostriction, from 5 to 500 K. The magnetic ordering temperature in $Fe_{2.5}InSn_{0.5}O_6$ (~432 K) is close to that observed for $InFeO_3$ (545 K)[55] but much higher than that of β-Mn_2InSbO_6,[54] presumably reflecting strong Fe−O superexchange interactions. The origin of the small ferromagnetic component observed in magnetic susceptibility measurements may be the same as that suggested for a similarly small FM component in $InFeO_3$ (weak ferromagnetism due to Dzaloshinskii−Moriya interactions in this noncentrosymmetric structure giving a slight canting of Fe^{3+} moments away from this collinear structure).[55] However, our NPD data are not sensitive to such subtle canting.

https://doi.org/10.1021/acs.chemmater.2c00312
Chem. Mater. 2022, 34, 5020−5029

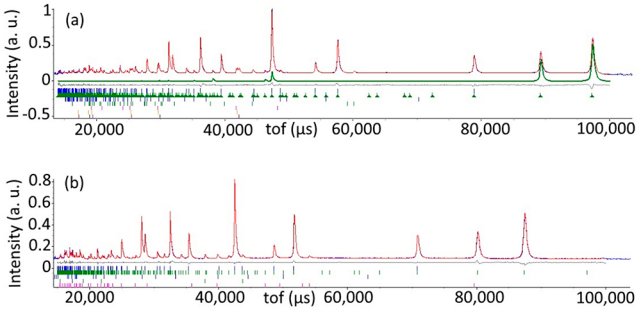

Figure 9. Refinement profiles for Rietveld refinement using 5 K NPD data for $Fe_{2.5}InSn_{0.5}O_6$ with the *R*3*c* model showing (a) bank 5 (153°) data and (b) bank 4 (122°) data. R_{wp} = 2.24%. R_p = 1.92%. χ^2 = 7.04. Observed, calculated, and difference profiles are colored blue, red, and gray, respectively, and magnetic scattering is highlighted in green. For panel a, and top (blue), upper (green), middle (blue), middle (green), middle (pink), lower (yellow), and bottom (purple) tick marks indicate reflection positions for $Fe_{2.5}InSn_{0.5}O_6$, a magnetic phase, a SnO_2 impurity (main peak at ∼44000 μs, 2.14 Å), an $InFe_2O_4$ phase (main peak at ∼44000 μs, 2.14 Å), Al from the sample environment (main peak at ∼42000 μs, 2.01 Å), Al from the sample environment (main peak at ∼42000 μs, 2.03 Å), and Al from the sample environment (main peak at ∼42000 μs, 2.04 Å), respectively. For panel b, top (blue), upper (green), middle (blue), middle (green), and lower (pink) tick marks indicate reflection positions for $Fe_{2.5}InSn_{0.5}O_6$, a magnetic phase, a SnO_2 impurity (main peak at ∼40000 μs, 2.14 Å), Al from the sample environment (main peak at ∼38000 μs, 2.04 Å), and an $InFe_2O_4$ phase (main peak at ∼54000 μs, 2.14 Å), respectively.

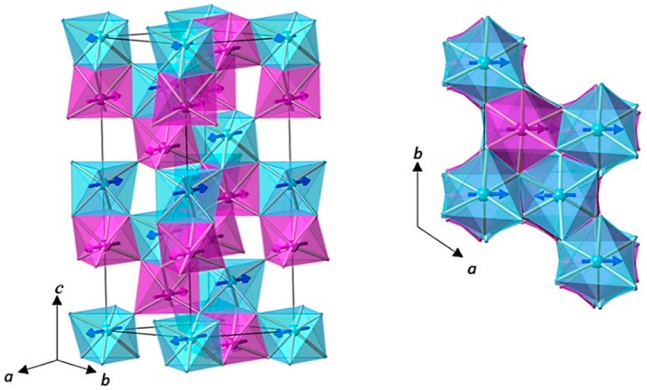

Figure 10. Illustration of the magnetic structure of $Fe_{2.5}InSn_{0.5}O_6$ from Rietveld refinement using 5 K NPD data. Cation sites 1 and 2 are colored purple and blue, respectively, and moments represented by arrows. Oxide sites have been omitted for the sake of clarity, and the blue arrows on the *a*−*b* plane view (right) have been shortened to show the purple arrows below.

CONCLUSION

In conclusion, we have studied the magnetic and structural properties of three new double corundum compounds, $Fe_{3-x}InSn_xO_6$ (x = 0, 0.25, and 0.5), prepared at a high pressure and high temperatures (6 GPa and 1400−1450 °C). All three phases order antiferromagnetically well above room temperature, with T_N values of 608, 532, and 432 K for x = 0, 0.25, and 0.5, respectively. Powder neutron diffraction investigations of x = 0.5 indicate that their magnetic structure consists of ferromagnetic layers stacked antiferromagnetically along [001]. $Fe_{3-x}InSn_xO_6$ is sensitive to small substitutions, with just 6.25% Sn^{4+} admixture enough to change the space group from centrosymmetric $R\bar{3}c$ to noncentrosymmetric *R*3*c*, as confirmed by temperature-dependent SHG measurements that showed an SHG response for x = 0.25 and 0.5 over the entire temperature measurement range (300−500 °C). Thus, the x = 0.25 and 0.5 phases are multifunctional, or possibly multiferroic. Temperature-dependent SHG measurements show a peak at T_N for x = 0.25 and 0.5, as does the specific heat for x = 0.5, which suggests coupling between polarization and magnetization. A hysteretic SHG response is observed, as would be expected in a ferroelectric material. Further studies, such as piezoforce microscopy or polarization-field and switching current measurements, would be of interest for exploring possible ferroelectric behavior and the origin of magnetoelectric coupling. These new compounds could lead to similar new multiferroic materials with high temperature functionality in the pursuit of magnetoelectric coupling.

ASSOCIATED CONTENT

Supporting Information

The Supporting Information is available free of charge at https://pubs.acs.org/doi/10.1021/acs.chemmater.2c00312.

Detailed structure and neutron refinements, transport data, room-temperature SHG figures, microprobe analysis data, and additional figures for x = 0.25 and 0 magnetization (PDF)

Crystallographic information file for x = 0 (CIF)

Crystallographic information file for x = 0.25 (CIF)

Crystallographic information file for x = 0.5 (CIF)

AUTHOR INFORMATION

Corresponding Author

Martha Greenblatt − *Department of Chemistry and Chemical Biology, Rutgers, The State University of New Jersey, Piscataway, New Jersey 08854, United States;* orcid.org/0000-0002-1806-2766; Email: greenbla@chem.rutgers.edu

Authors

Corey E. Frank − *Department of Chemistry and Chemical Biology, Rutgers, The State University of New Jersey, Piscataway, New Jersey 08854, United States;* Present Address: C.E.F.: National Institute of Standards and Technology, Center for Neutron Research, Gaithersburg, MD 20899; orcid.org/0000-0003-2638-7795

Emma E. McCabe − *Department of Physics, Durham University, Durham DH1 3LE, United Kingdom;* orcid.org/0000-0001-5868-4570

Fabio Orlandi − *ISIS Facility, STFC, Rutherford Appleton Laboratory, Chilton, Oxfordshire OX11 0QX, United Kingdom;* orcid.org/0000-0001-6333-521X

Pascal Manuel − *ISIS Facility, STFC, Rutherford Appleton Laboratory, Chilton, Oxfordshire OX11 0QX, United Kingdom*

Xiaoyan Tan − *Department of Chemistry and Biochemistry, George Mason University, Fairfax, Virginia 22030, United States;* orcid.org/0000-0002-1742-8252

Zheng Deng − *Institute of Physics, School of Physics, University of Chinese Academy of Sciences, Beijing 100190, P. R. China*

Changqing Jin − *Institute of Physics, School of Physics, University of Chinese Academy of Sciences, Beijing 100190, P. R. China*

https://doi.org/10.1021/acs.chemmater.2c00312
Chem. Mater. 2022, 34, 5020−5029

Mark Croft − *Department of Physics and Astronomy, Rutgers, The State University of New Jersey, Piscataway, New Jersey 08854, United States*
Thomas Emge − *Department of Chemistry and Chemical Biology, Rutgers, The State University of New Jersey, Piscataway, New Jersey 08854, United States*
Shukai Yu − *Department of Materials Science and Engineering, The Pennsylvania State University, University Park, Pennsylvania 16802, United States*
Huaiyu Wang − *Department of Materials Science and Engineering, The Pennsylvania State University, University Park, Pennsylvania 16802, United States*
Venkatraman Gopalan − *Department of Materials Science and Engineering, The Pennsylvania State University, University Park, Pennsylvania 16802, United States*
Saul Lapidus − *Advanced Photon Source, Argonne National Laboratory, Lemont, Illinois 60439, United States*
MeiXia Wu − *MOE Key Laboratory of Bioinorganic and Synthetic Chemistry, School of Chemistry, Sun Yat-Sen University, Guangzhou 510275, China*
Man-Rong Li − *MOE Key Laboratory of Bioinorganic and Synthetic Chemistry, School of Chemistry, Sun Yat-Sen University, Guangzhou 510275, China;* orcid.org/0000-0001-8424-9134
Juliane Gross − *Department of Earth and Planetary Sciences, Rutgers, The State University of New Jersey, Piscataway, New Jersey 08854, United States*
Paul Burger − *Department of Earth and Planetary Sciences, Rutgers, The State University of New Jersey, Piscataway, New Jersey 08854, United States*
Aleksandra Mielewczyk-Gryń − *Faculty of Applied Physics and Mathematics and Advanced Materials Centre, Gdansk University of Technology, 80-233 Gdańsk, Poland;* orcid.org/0000-0001-6795-3840
Tomasz Klimczuk − *Faculty of Applied Physics and Mathematics and Advanced Materials Centre, Gdansk University of Technology, 80-233 Gdańsk, Poland;* orcid.org/0000-0002-7089-4631
Weiwei Xie − *Department of Chemistry and Chemical Biology, Rutgers, The State University of New Jersey, Piscataway, New Jersey 08854, United States;* orcid.org/0000-0002-5500-8195
David Walker − *Lamont Doherty Earth Observatory, Columbia University, Palisades, New York 10964, United States*

Complete contact information is available at: https://pubs.acs.org/10.1021/acs.chemmater.2c00312

Funding

M.G. and X.T. were supported by the Center for Computational Design of Functional Strongly Correlated Materials and Theoretical Spectroscopy under U.S. Department of Energy (DOE) Grant DE-FOA0001276. The XANES work used beamline 7-BM (QAS) of the National Synchrotron Light Source II, a U.S. DOE Office of Science User Facility operated for the DOE Office of Science by Brookhaven National Laboratory under Contract DE-SC0012704. The authors acknowledge the Science and Technology Facility Council (U.K.) for the provision of neutron beam time at the ISIS facility on the WISH instrument (DOI: 10.5286/ISIS.E.RB1920145). M.-R.L. and M.W. were supported by the National Natural Science Fund of China (NSFC-11804404). V.G., S.Y., and H.W. acknowledge support from the National Science Foundation MRSEC Center for Nanoscale Science (DMR-2011839). Use of the Advanced Photon Source at Argonne National Laboratory was supported by the DOE, Office of Science, Office of Basic Energy Sciences, under Contract DE-AC02-06CH11357. W.X. was supported by the DOE, Office of Science, Office of Basic Energy Sciences, under Contract DE-0000262057.

Notes

The authors declare no competing financial interest.
Identification of commercial equipment does not imply recommendation or endorsement by NIST.

■ ACKNOWLEDGMENTS

The authors thank Ms. Jean Hanley for making the high-pressure assemblies. The support of A. Fiege during the electron microprobe analyses at the American Museum of Natural History was greatly appreciated. The authors also thank J. Anderson for her help during the electron backscatter diffractometry at The Pennsylvania State University. The invaluable help of the QAS beamline scientists S. Ehrlich and S. Khalid is gratefully acknowledged. Portions of this work were published in ref 56.

■ DEDICATION

This manuscript is dedicated in honor of the 100th birthday of Dr. John B. Goodenough.

■ REFERENCES

(1) Schmid, H. Multi-ferroic magnetoelectrics. *Ferroelectrics* **1994**, *162*, 317−338.
(2) Cai, G.-H.; Greenblatt, M.; Li, M.-R. Polar Magnets in Double Corundum Oxides. *Chem. Mater.* **2017**, *29*, 5447−5457.
(3) Zarzuela, R.; Kim, S. K.; Tserkovnyak, Y. Magnetoelectric antiferromagnets as platforms for the manipulation of solitons. *Phys. Rev. B* **2018**, *97*, No. 014418.
(4) Halley, D.; et al. Size-induced enhanced magnetoelectric effect and multiferroicity in chromium oxide nanoclusters. *Nat. Commun.* **2014**, *5*, 3167.
(5) Nan, C.-W.; Bichurin, M. I.; Dong, S.; Viehland, D.; Srinivasan, G. Multiferroic magnetoelectric composites: Historical perspective, status, and future directions. *J. Appl. Phys.* **2008**, 031101.
(6) Hill, N. A. Why Are There so Few Magnetic Ferroelectrics? *J. Phys. Chem. B* **2000**, *104*, 6694−6709.
(7) von Hippel, A. Ferroelectricity, Domain Structure, and Phase Transition of Barium Titanate. *Rev. Mod. Phys.* **1950**, *22*, 221−237.
(8) Khomskii, D. I. Multiferroics: Different ways to combine magnetism and ferroelectricity. *J. Mag Mag Mater.* **2006**, *306*, 1−8.
(9) Benedek, N. A.; Rondinelli, J. M.; Djani, H.; Ghosez, P.; Lightfoot, P. Understanding ferroelectricity in layered perovskites: new ideas and insights from theory and experiments. *Dalton Trans* **2015**, *44*, 10543−10558.
(10) Ye, M.; Vanderbilt, D. Ferroelectricity in corundum derivatives. *Phys. Rev. B* **2016**, *93*, No. 134303.
(11) McCabe, E. E. In *Reference Module in Chemistry, Molecular Sciences and Chemical Engineering*; Elsevier, 2022.
(12) Ivanov, S. A.; et al. Spin and Dipole Ordering in Ni_2InSbO_6 and Ni_2ScSbO_6 with Corundum-Related Structure. *Chem. Mater.* **2013**, *25*, 935−945.
(13) Zupan, J.; Kolar, D.; Urbanc, V. Magnetic Properties of Ni_3TeO_6. *Mater. Res. Bull.* **1971**, *6*, 1353−1359.
(14) Solana-Madruga, E.; et al. High pressure synthesis of polar and non-polar cation-ordered polymorphs of Mn_2ScSbO_6. *Dalton Trans* **2015**, *44*, 20441−20448.

(15) Li, M. R.; et al. Designing Polar and Magnetic Oxides: Zn_2FeTaO_6 - in Search of Multiferroics. *J. Am. Chem. Soc.* **2014**, *136*, 8508−8511.
(16) Song, G.; Zhang, W. Comparative studies on the room-temperature ferrielectric and ferrimagnetic Ni_3TeO_6-type A_2FeMoO_6 compounds (A = Sc, Lu). *Sci. Rep.* **2016**, *6*, 20133.
(17) Li, M. R.; et al. Magnetic-Structure-Stabilized Polarization in an Above-Room-Temperature Ferrimagnet. *Angew. Chem. Int. Ed* **2014**, *53*, 10774−10778.
(18) Li, M.-R.; et al. Magnetostriction-polarization coupling in multiferroic Mn_2MnWO_6. *Nat. Commun.* **2017**, *8*, 2037.
(19) Li, M. R.; et al. Low-Temperature Cationic Rearrangement in a Bulk Metal Oxide. *Angew. Chem., Int. Ed.* **2016**, *55*, 9862−9867.
(20) Li, M. R.; et al. Polar and magnetic Mn_2FeMO_6 (M = Nb, Ta) with $LiNbO_3$-type structure: high-pressure synthesis. *Angew. Chem., Int. Ed. Engl.* **2013**, *52*, 8406−8410.
(21) Li, M. R.; et al. Mn_2FeWO_6: A new Ni_3TeO_6-type polar and magnetic oxide. *Adv. Mater.* **2015**, *27*, 2177−2181.
(22) Živković, I.; Prša, K.; Zaharko, O.; Berger, H. Ni_3TeO_6—a collinear antiferromagnet with ferromagnetic honeycomb planes. *J. Phys.: Condens. Matter* **2010**, *22*, No. 056002.
(23) Megaw, H. A note on the structure of lithium niobate, $LiNbO_3$. *Acta Crystallogr. A* **1968**, *24*, 583−588.
(24) Nassau, K.; Levinstein, H. J.; Loiacono, G. M. Ferroelectric lithium niobate. 1. Growth, domain structure, dislocations and etching. *J. Phys. Chem. Solids* **1966**, *27*, 983−988.
(25) Chen, W.-t.; et al. Robust Antiferromagnetism and Structural Disorder in BixCa1−xFeO3 Perovskites. *Chem. Mater.* **2009**, *21*, 2085−2093.
(26) Li, M.-R.; et al. A Polar Corundum Oxide Displaying Weak Ferromagnetism at Room Temperature. *J. Am. Chem. Soc.* **2012**, *134*, 3737−3747.
(27) Niu, H.; et al. Room Temperature Magnetically Ordered Polar Corundum $GaFeO_3$ Displaying Magnetoelectric Coupling. *J. Am. Chem. Soc.* **2017**, *139*, 1520−1531.
(28) Fujita, K.; et al. $LiNbO_3$-Type $InFeO_3$: Room-Temperature Polar Magnet without Second-Order Jahn−Teller Active Ions. *Chem. Mater.* **2016**, *28*, 6644−6655.
(29) Gaudon, M.; et al. Influence of Sn^{4+} and Sn^{4+}/Mg^{2+} doping on structural features and visible absorption properties of α-Fe_2O_3 hematite. *J. Solid State Chem.* **2010**, *183*, 2101−2109.
(30) Sheldrick, G. *Twinabs*; University of Göttingen: Göttingen, Germany, 2009.
(31) Sheldrick, G. M. *SHELXT-2014/5*; University of Göttingen: Göttingen, Germany, 2014.
(32) Sheldrick, G. M. Crystal structure refinement with *SHELXL*. *Acta Crystallogr., Sect C* **2015**, *71*, 3−8.
(33) Chapon, L. C.; et al. Wish: The New Powder and Single Crystal Magnetic Diffractometer on the Second Target Station. *Neutron News* **2011**, *22*, 22.
(34) Rietveld, H. M. Rietveld refinement. *J. Appl. Crystallogr.* **1969**, *2*, 65.
(35) Coelho, A. A. Topas. *J. Appl. Crystallogr.* **2003**, *36*, 86.
(36) *Topas Academic: General profile and structure analysis software for powder diffraction data*; Bruker AXS: Karlsruhe, Germany, 2012.
(37) Campbell, B. J.; Stokes, H. T.; Tanner, D. E.; Hatch, D. M. ISODISTORT. *J. Appl. Crystallogr.* **2006**, *39*, 607−614.
(38) Nespolo, M.; Ferraris, G. Applied geminography - symmetry analysis of twinned crystals and definition of twinning by reticular polyholohedry. *Acta Crystallogr. A* **2004**, *60*, 89−95.
(39) Kim, S. W.; et al. $YCrWO_6$: Polar and Magnetic Oxide with $CaTa_2O_6$-Related Structure. *Chem. Mater.* **2018**, *30*, 1045−1054.
(40) Wang, J.; et al. Temperature-dependent phase transition in barium titanate crystals probed by second harmonic generation. *Appl. Phys. Lett.* **2018**, *112*, 102904.
(41) Sommer, D.; Friese, D.; Kleemann, W.; Rytz, D. Ferroelectric phase transitions and domain relaxation in $KTa_{1-x}Nb_xO_3$. *Ferroelectr* **1991**, *124*, 231−236.
(42) Kim, J. H.; Kim, M.; Kim, S. B.; Hahn, J. H. Temperature-dependent second harmonic generation in $^6LiRbSO_4$ and $^7LiRbSO_4$. *Solid State Commun.* **1996**, *98*, 241−244.
(43) Miller, R. C.; Savage, A. Temperature dependence of the optical properties of ferroelectric $LiNbO_3$ and $LiTaO_3$. *Appl. Phys. Lett.* **1966**, *9*, 169−171.
(44) Morrish, A. H. *Canted antiferromagnetism: hematite*; World Scientific Publishing: Singapore, 1994.
(45) Catti, M.; Valerio, G.; Dovesi, R. Theoretical study of electronic, magnetic, and structural properties of α-Fe_2O_3 (hematite). *Phys. Rev. B* **1995**, *51*, 7441−7450.
(46) Bozorth, R. M.; Walsh, D. E.; Williams, A. J. Magnetization of Ilmenite-Hematite System at Low Temperatures. *Phys. Rev.* **1957**, *108*, 157−158.
(47) Lin, S. T. Magnetic Properties of Hematite Single Crystals. I. Magnetization Isotherms, Antiferromagnetic Susceptibility, and Weak Ferromagnetism of a Natural Crystal. *Phys. Rev.* **1959**, *116*, 1447−1452.
(48) Haigh, G. Observations on the magnetic transition in hematite at-15° C. *Philos. Mag.* **1957**, *2*, 877−890.
(49) Kawamoto, T.; et al. Room-Temperature Polar Ferromagnet $ScFeO_3$ Transformed from a High-Pressure Orthorhombic Perovskite Phase. *J. Am. Chem. Soc.* **2014**, *136*, 15291−15299.
(50) Glazer, A. The classification of tilted octahedra in perovskites. *Acta Crystallogr. B* **1972**, *28*, 3384−3392.
(51) Martínez-Lope, M. J.; Alonso, J. A.; Retuerto, M.; Fernández-Díaz, M. T. Evolution of the crystal structure of RVO_3 (R = La, Ce, Pr, Nd, Tb, Ho, Er, Tm, Yb, Lu, Y) perovskites from neutron powder diffraction data. *Inorg. Chem.* **2008**, *47*, 2634−2640.
(52) Feng, H. L.; Yamaura, K.; Tjeng, L. H.; Jansen, M. The role of nonmagnetic d^0 vs. d^{10} B-type cations on the magnetic exchange interactions in osmium double perovskites. *J. Solid State Chem.* **2016**, *243*, 119−123.
(53) Shirane, G. A note on the magnetic intensities of neutron powder diffraction. *Acta Crystallogr.* **1959**, *12*, 282−285.
(54) Arévalo-López, Á. M.; et al. Evolving spin periodicity and lock-in transition in the frustrated ordered ilmenite-type β-Mn_2InSbO_6. *Phys. Rev. B* **2018**, *98*, 214403.
(55) Fujita, K.; et al. $LiNbO_3$-type $InFeO_3$: room-temperature polar magnet without second-order Jahn-Teller active ions. *Chem. Mater.* **2016**, *28*, 6644−6655.
(56) Frank, C. E. Design and Synthesis of Perovskites and Corundum Derivatives with Unusual Magnetic, Electronic, and Structural Coupling. Doctoral Dissertation, Rutgers, The State University of New Jersey, New Brunswick, NJ, 2021.

https://doi.org/10.1021/acs.chemmater.2c00312
Chem. Mater. 2022, 34, 5020−5029